

Refael Fadida¹

Rafael,
POB 2250,
Haifa 3102102, Israel
e-mail: fadidarafi@gmail.com

Daniel Rittel

Faculty of Mechanical Engineering,
Technion, Haifa 3200003, Israel
e-mail: rittel@me.technion.ac.il

Amnon Shirizly

Rafael,
POB 2250,
Haifa 3102102, Israel
e-mail: a.shirizly@gmail.com

Dynamic Mechanical Behavior of Additively Manufactured Ti6Al4V With Controlled Voids

The mechanical properties of additively manufactured (AM) dense and porous Ti6Al4V specimens were investigated under static and dynamic compression. The fully dense specimens were fabricated using laser melting process. The porous specimens contained spherical pores with full control on the geometry and location of the pores. The laser processed dense material exhibited superior strength in the static and dynamic tests, compared to the same conventional material, but the ductility of the two was comparable. Single pore specimens exhibited a linear relationship between the load and the pore volume fraction. The comparison between single- and double-pore specimens, at identical volume fractions, revealed the importance of the pores' orientation with respect to the applied load. [DOI: 10.1115/1.4029745]

Keywords: additive manufacturing, porous materials, dynamic behavior, Ti6Al4V

1 Introduction

Titanium and its alloys are used in numerous applications due to their superior properties, such as high strength to weight ratio and corrosion resistance. The most common applications include aerospace, military, chemical, biomedical, industrial processes, and so on. Veiga et al. [1] presented a review on titanium alloys with emphasis on Ti6Al4V and its applications. According to these authors, the tensile strength of titanium alloys varies normally from about 200 Mpa for pure titanium to about 1400 Mpa for near- β alloys, while for Ti6Al4V the values range between 900 and 1200 Mpa. The mechanical behavior of titanium has been extensively addressed, statically, and dynamically in many researches. Nicholas [2] reported the stress-strain curves of several titanium alloys, including Ti6Al4V at different strain rates. According to Nicholas [2], all the titanium alloys show an increase in flow stress with strain rate, with the degree of rate sensitivity apparently increasing slightly at the higher strain rates. A similar behavior was reported by Wulf [3]. Today's technology makes it possible to produce metal parts in printlike method. The raw material is powder, and processes, such as Direct Metal Laser Sintering (DMLSTM), are usually utilized to solidify the part. In general, the full-melt powder bed fusion describes processes, which are used to manufacture of fully dense metallic parts. Its specifications for Ti6Al4V are covered in detail at ASTM F2924-14 [4]. The idea of full melting is supported by the continuously improved laser processing conditions in recent years, such as higher power lasers, smaller focused spot size, and smaller layer thickness, all leading to significantly improved microstructural and mechanical properties [5,6]. The 3D-printing or AM technology represents a variety of processes in which any geometry, complex as it may be, can be processed from a 3D computer model (CAD). AM enables production of custom-made geometries, which are often impossible or too costly to manufacture using conventional methods. Optimization of parts for a maximum strength-to-weight ratio is one application of AM technology that has a major importance in the design of aircrafts. Many types of metals are suitable and available for printing such as titanium, aluminum, and their alloys. The main drawbacks of the technology are its

high price, surface finish, and part's size (limited by machine size). In this technology, the part is elaborated by adding ultrathin layers (hence the name AM) of molten material one by one. A high-power laser melts the pattern in each layer, then the part is slightly lowered, a new layer of powder is applied, and so on until completion. Dense areas are fully melted, while others (i.e., voids) remain in powdery state. From a materials mechanics perspective, it is interesting consider these inner voids as "pores" of controlled dimensions and location. Controlled porosity is a unique feature of this technology, which allows the study of pore behavior under loadings. Such a study has not yet been carried out due to the lack of adequate technology to produce *fully enclosed pores*. Many researches have addressed the static and dynamic behavior of porous materials, both experimentally and theoretically. Constitutive equations for porous ductile solids were developed based on homogenization theory [7]. Gurson [8] developed in the midseventies, a seminal model for porous ductile materials, which suggests an approximate yield criteria and flow rules regarding spherical and cylindrical voids. Gurson's criterion was based on a single variable, which is the volume fraction of the voids denoted as f [8]. A few years later, Tvergaard [9] suggested an adjustment of Gurson's constitutive relations. Many studies have extended and modified the classical Gurson's model (e.g., Refs. [10] and [11]), and a detailed review of up to date models can be found in Benzerga and Leblond [7]. While all the above-mentioned references (and many unmentioned here for the sake of brevity) address essentially quasi-static regimes, much less is known about the high strain rate plastic response of porous materials. Silva and Ramesh [12] showed ~20% decrease in the yield strength (in compression) for a sintered porous Ti6Al4V with a porosity of 7.6%. Publications concerning porous materials fabricated by AM, and subjected to dynamic loading, are still quite scarce. Biswas et al. [13] investigated the deformation of Ti6Al4V alloy processed by the Laser Engineered Net Shaping (LENSTM) system. This technology is based on sprayed particles that pass through a laser source and then solidify on a substrate. The porous material created by varying the process's parameters such as laser power, laser scanning speed, and the powder feed rate. According to these authors, 20% porous Ti6Al4V showed lower strength, but higher ductility compared to 10% material, but 10% porous material had both less strength and ductility than dense material (0% porosity). In a continuation of this study, Biswas and Ding [14] carried out a numerical investigation of the dynamic behavior of Ti6Al4V for discrete cases of porosity. Their study indicates that pore can

¹Corresponding author.

Contributed by the Applied Mechanics Division of ASME for publication in the JOURNAL OF APPLIED MECHANICS. Manuscript received November 25, 2014; final manuscript received February 4, 2015; published online February 26, 2015. Assoc. Editor: Weinong Chen.

Table 1 Experimental parameters

Parameter	Value	Units
L	2000	mm
D	19.3	mm
l_0	7.0	mm
d_0	7.0	mm
L/D	104	—
D/d_0	2.75	—
l_0/d_0	1	—

serve as both failure initiator and inhibitor, namely, lower strength due to higher stress concentration, but higher apparent ductility due to slower failure propagation. From the above literature survey, it appears that an adequate technique of controlled fabrication of voids is still desirable to describe well the behavior of pores experimentally and to support numerical and theoretical studies.

2 Experimental Setup

2.1 Dynamic Compression Tests. The experimental method used in this present research is the split Hopkinson pressure bar (SHPB), which is a standard test for high strain rate materials characterization in compression [15,16]. Table 1 summarizes the nominal ratios of the SHPB apparatus, which are acceptable for dynamic compression tests [17]. L and D indicate the length and the diameter of the bars, respectively. l_0 and d_0 indicate the initial length and diameter of the specimen, respectively.

2.2 Dynamic Compression Specimens.

2.2.1 Manufacturing. In AM process, the part is built on metal platform that supports it during localized surface melting by a scanning laser. A 30 μm layer of Ti6Al4V powder is spread on the platform, which is melted by the laser according to the part's design. The process is repeated layer by layer until the final part's height is achieved. The unexposed powder is then discarded, and the manufactured part is then disconnected mechanically from its supporting basis. Figure 1(a) shows an example of a batch of specimens at the end of the manufacturing process. Wire erosion was used to separate the specimens from the substrate. The specimens were marked in order to distinguish between series of specimens in the wire erosion process. Each specimen was cut a few millimeters far from the material edges, as shown in Fig. 1(b) to ensure no edge effect. The cylindrical face was left untouched, but the cylinder's flat surfaces were lathe machined to achieve high surface quality and parallelism, which are all necessary for high accuracy and repeatability of the results [16]. A set of five cylindrical specimens $\varnothing 7 \times 7 \text{ mm}$ were compressed. The specimens were designed to be almost identical in their geometrical dimensions. The typical tolerance for specimen's length and

diameter was of the order of $\pm 0.02 \text{ mm}$. A set of five specimens $\varnothing 7 \times 3.5$ were used only to achieve the highest reported strain rate (7000 s^{-1}). Figure 1(c) shows a typical compression specimen by the end of all manufacturing stages. The specimens for the dynamic tests were used also for the quasi-static tests. The quasi-static test was carried out using a servohydraulic machine (MTS 810). The displacements were measured using an optical extensometer.

2.2.2 Single and Double Pore Specimens. As mentioned before, the AM technology allows the fabrication of a porous material in a controlled manner. Usually, when porous material is considered, it is meant that the material contains a large amount of randomly distributed voids. Controlled porosity here relates to the ability to create voids inside the material, of an arbitrary shape, dimensions, location, and pattern, all that with a relatively high geometrical accuracy. This study seeks to examine *simple cases* of porosity that can serve as a tool for predicting the behavior of a pattern. Each specimen defined as a unit cell that theoretically can represent a part of multipore case. Spherical void was chosen to represent a pore for practical reasons. The porous specimens were designed using CAD software. The spherical voids were modeled inside the specimen, with the desired dimensions and locations. Porous and fully dense specimens had similar dimensions ($\varnothing 7 \times 7 \text{ mm}$). Two main types of porous specimen were manufactured and tested. The first type is a single pore specimen where the pore is located at the geometric center of the specimen, as shown in Fig. 2. The second type is a double pore specimen where the pores are located in three different orientations, as shown in Fig. 3. The main point in manufacturing a single pore specimen was to explore the change in strength as a function of pore size or as a function of its volume fraction. The volume fraction is a dimensionless number and a well-known parameter in studies dealing with porous materials [8]. The single pore specimens were manufactured with an internal pore in varying diameter in the range of $\varnothing 1$ – $\varnothing 3 \text{ mm}$. The corresponding volume fraction was 0.2–5.2%, respectively. Table 2 summarizes the parameters of the porous specimens. The manufacturing process leaves inner closed volume untouched (i.e., not melted by the laser), which means that powder (i.e., the raw material) remains trapped inside the pore, as shown in Fig. 4(a). This residual powder was assumed to have negligible effect on tests results. The basis to this assumption is that powder transmits stress waves in a very poor manner compared to solids [18]. Moreover, it was assumed that fracture due to the existence of inner pore happens before the powder compression. Figure 4(b) shows a cross section of a single pore specimen in which the residual powder inside the pore was manually removed. Since the (inner) pores are not visible, a verification of pores existence was done using X-ray imaging, as shown in Fig. 5.

Three types of double pore specimen were manufactured, namely, along the symmetry axis—*axial*, along radial direction—

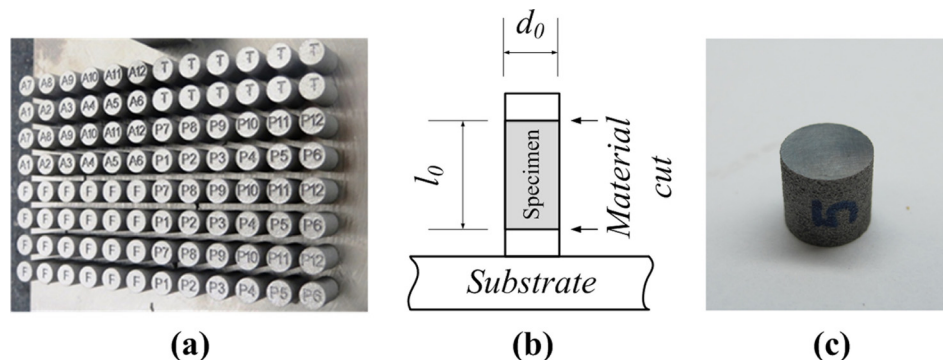


Fig. 1 (a) An example of a batch of specimens, (b) wire cutting of specimen, and (c) compression specimen

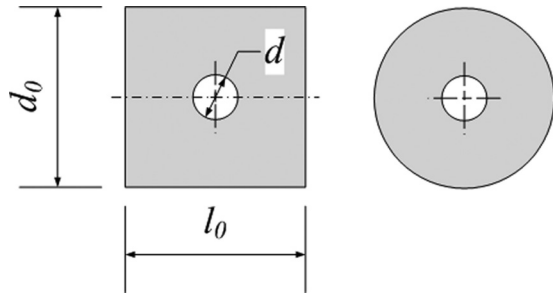


Fig. 2 Single pore specimen

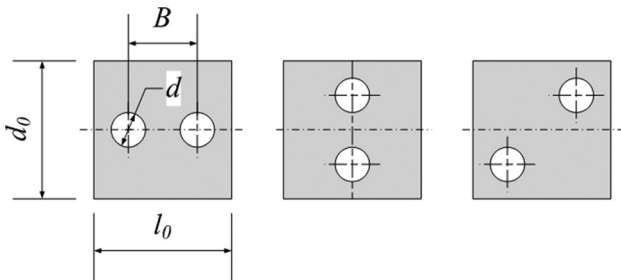


Fig. 3 Double pore specimen: axial, lateral, and diagonal, respectively, from left to right

lateral, and at 45deg with respect to the longitudinal axis—*diagonal*. The double pore specimens were designed in a manner that the volume fraction of both pores is identical to the volume fraction of a single pore. A dimensionless ratio was set to describe the pore size in relation to the distance between pores named as d/B ratio. The pore diameter was kept constant ($d = \text{Ø}1.6 \text{ mm}$), while several values of distance between pores (B) were chosen, namely, d , $d/2$, and $d/4$. A low d/B ratio means pores are quite “far” from each other, while high ratio means that the pores are quite “close” to each other. Figure 6 shows an X-ray image of the axial double pore specimen, at various d/B ratios. The volume fraction of all double pores specimen types was equal to 1.6%, which is the same as the average volume fraction of a single pore set. Each type of specimen was tested 3–5 times, to certain repeatability in the measured results.

2.2.3 Data Reduction. For a homogeneous specimen, the stress is linearly related to the cross section when the latter is constant. However, stress and strain variations are caused by a presence of pores. Therefore, the results cannot be shown in terms of stress–strain curves, and throughout this work we consistently report measured forces and displacements for the porous specimens, which do not depend on the specimen’s geometry. Given the fact that all specimens have almost identical dimensions,

Table 2 Parameters of porous specimens

Parameter	Value	Units
Single pore specimen		
l_0	7.0	mm
d_0	Ø7.0	mm
d	Ø1.0, Ø1.5, Ø2.0, Ø2.5, Ø3.0	mm
Double pore specimen		
l_0	7.0	mm
d_0	Ø7.0	mm
d	Ø1.6	mm
B	1.6, 0.8, 0.4	mm
d/B	1, 2, 4	—
f	0.2, 0.7, 1.6, 3.0, 5.2	%

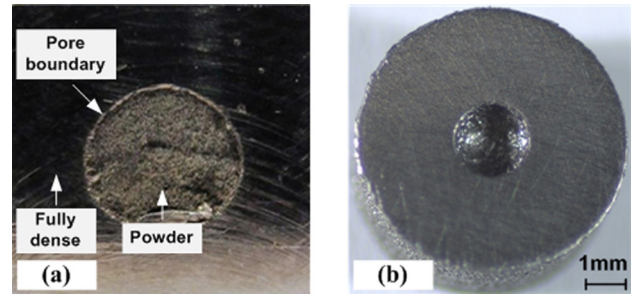


Fig. 4 A cross section of a single pore specimen. (a) An example of residual powder inside a pore. (b) A Ø2 mm pore, after the powder removal. Note the relatively accurate geometry of the spherical pore.

comparisons between various pore contents can be established without any ambiguity related to the inhomogeneous cross section of specimens. An example of dynamic force equilibrium is given in Fig. 7. Such state of equilibrium was ascertained for each dynamic test. It should be noted that whereas the forces are in equilibrium, this does not necessarily imply stress uniformity in the specimen, as a result of the stress wave loading of the specimen. However, as mentioned before, we will not characterize stresses throughout this work so that we will not further deal with this issue. Based on force equilibrium considerations, the applied load will be identified as F-out from thereon.

3 Experimental Results

3.1 Quasi-Static Compression of Fully Dense Ti6Al4V.

The quasi-static compression experiments were carried out to measure the mechanical properties of the printed material and compare them to the conventional material. The strain rate for this test was set to $1 \times 10^{-3} \text{ s}^{-1}$, which is typical of quasi-static experiments [3]. An 18 mm thick, cold rolled annealed plate of premium-quality Ti6Al4V was chosen to represent the conventionally processed material, to be later compared with the printed material. Figure 8 shows the comparison between printed (AM) and conventional Ti6Al4V.

As can be seen, the printed material’s compressive strength is much higher than that of the conventionally processed material. The measured difference exceeds 35% for the printed material at $\varepsilon = 0.1$. A slight difference in elastic moduli can be noticed, but is deemed to be more related to the test accuracy than to the actual material property. The printed specimens failed by shear as shown in Fig. 9 at $\varepsilon = 0.17$, while the conventionally processed specimens did not fail at the same strain. The printed material reaches its full strength sooner than the conventional material, which indicates a limited strain hardening capacity. The compressive strength of the printed material was found to be of almost 1400 Mpa at $\varepsilon = 0.1$ as compared to about 1000 Mpa at the same strain rate for the conventional material.

3.2 Dynamic Compression of Fully Dense Ti6Al4V. A set of 30 fully dense cylindrical specimens were tested at several strain rates in the range of $2 \times 10^3 - 7 \times 10^3 \text{ s}^{-1}$. At each strain rate, 3–5 specimens were tested, to ensure repeatability. A set of three specimens made of conventionally processed material were tested for comparison at the same strain rate. Figure 10 shows the typical stress–strain curves of several specimens tested at a nominal strain rate of $2 \times 10^3 \text{ s}^{-1}$.

Just like for the quasi-static results, the dynamic behavior of the printed material exhibits better performance in strength as compared to the conventionally processed material. The measured difference exceeds 20% in favor of the printed material at $\varepsilon = 0.1$. Both conventional and printed specimens failed by shear at approximately $\varepsilon = 0.2$, as shown in Fig. 10. Here, one must note

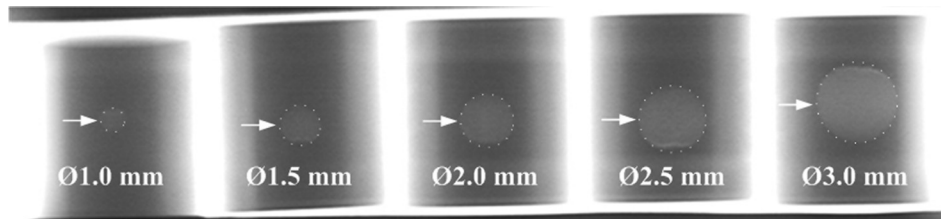


Fig. 5 A set of single pore specimens in X-ray image

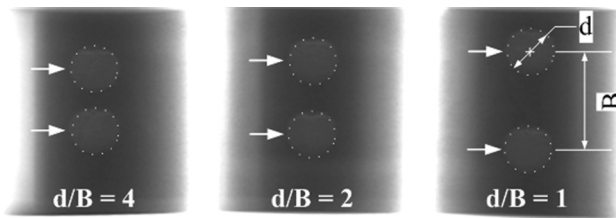


Fig. 6 X-ray image of axial double pore specimen with varying d/B ratio

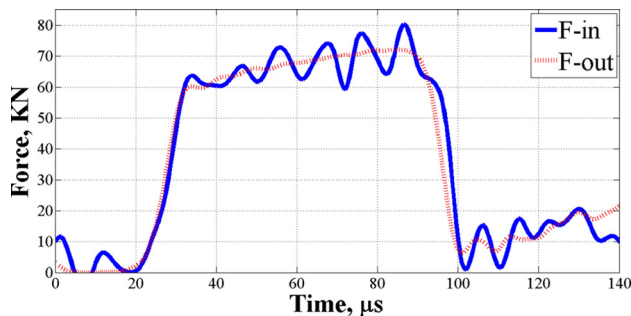


Fig. 7 Typical force equilibrium of printed Ti6Al4V specimen, in dynamic compression. F-in and F-out stand for incident and transmitted force, respectively.

that the concept of a failure strain in compression usually has a limited meaning, as compared to the better accepted notion of tensile failure strain. Tensile tests always end up in fracture, whereas compression tests, which involve extensive barreling at some stage, may not always end up by clear specimen fracture. However, in the present case, fracture of the AM compression specimens, whether static or dynamic, was associated with a well-defined state of shear localization. The printed material reaches to its flow strength sooner than the conventional material with hardly noticeable strain hardening compared to the conventionally processed material. The compressive strength of the printed material found to exceed 1500 MPa at $\varepsilon=0.1$. Both materials failed by

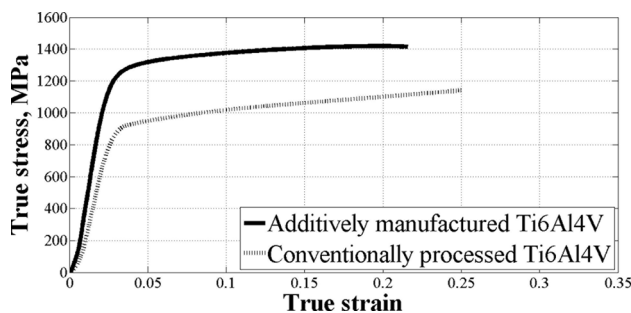


Fig. 8 Fully dense printed Ti6Al4V compared to conventional material in quasi-static compression at nominal strain rate of $1 \times 10^{-3} \text{ s}^{-1}$

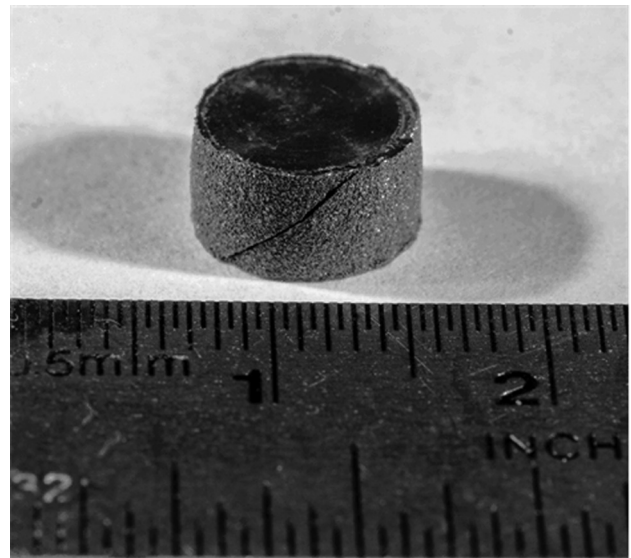


Fig. 9 Failure of printed Ti6Al4V specimen in quasi-static compression. Note the shear failure pattern.

(adiabatic) shear at 45 deg to the applied load, as shown in Fig. 11. Ti6Al4V is well-known to be prone to the formation of adiabatic shear bands and subsequent failure [19]. Fractographic analysis of failed specimens, to be reported later, confirms this observation.

The fracture surfaces of selected specimens were examined using the scanning electron microscope (SEM), as shown in Fig. 12. The observation of elongated dimples confirms beyond any doubt the operation of a dynamic shear failure mechanism for the AM material.

Most specimens were designed with an aspect ratio of 1 as mentioned previously. Higher strain rates were achieved using specimens with a lower aspect ratio. For l_0/d_0 ratio of 0.5, a maximum strain rate of $7 \times 10^3 \text{ s}^{-1}$ was reached. Figure 13 shows that at those high strain rates, no further elevation of the material's flow strength is observed, in accord with Nicholas'

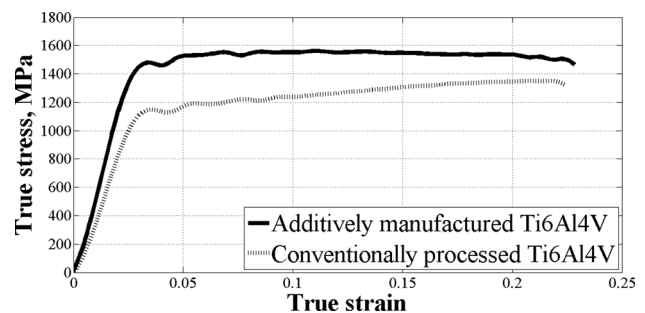


Fig. 10 Fully dense printed Ti6Al4V in dynamic compression compared to conventional material at nominal strain rate of $2 \times 10^{-3} \text{ s}^{-1}$

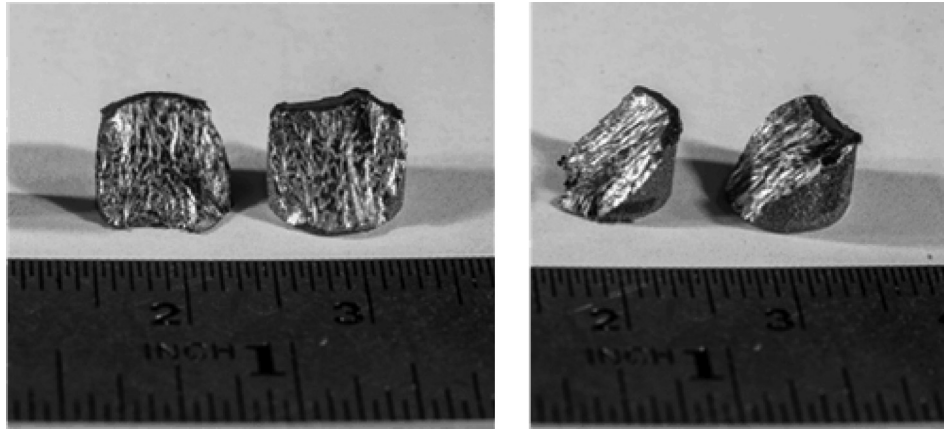


Fig. 11 Typical dynamic fracture of fully dense printed Ti6Al4V specimen. Note the shear fracture pattern.

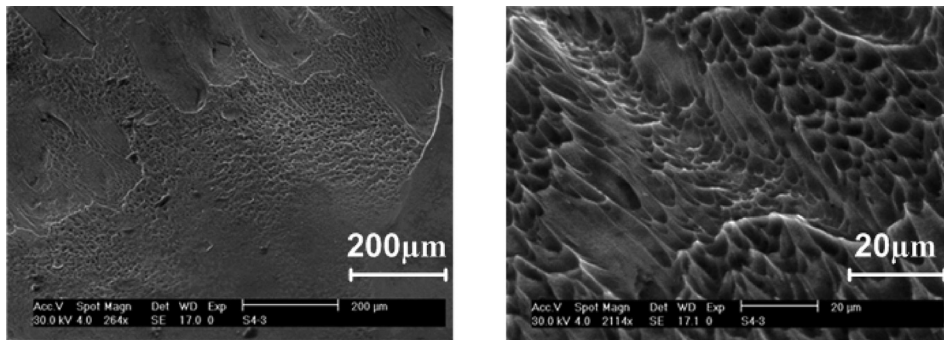


Fig. 12 SEM image of printed Ti6Al4V failure. Note the elongated dimples.

observations [2]. Yet, the previously mentioned lack of strain hardening becomes even more evident at $7 \times 10^3 \text{ s}^{-1}$. Interestingly, the failure strain was found to be comparable at all strain rates, an observation that matches well the operation of an adiabatic shear failure mechanism. Indeed, once set in, this mechanism develops rapidly, independently of the strain rate, as reported by Osovski et al. [20]. It should be noted that the strain rate sensitivity of printed Ti6Al4V was not further investigated in this research and remains to be studied in further work.

3.3 Dynamic Compression of Single Pore Specimen. As mentioned before, porous specimens' results will be deliberately presented as load versus displacement curves, instead of stress versus strain, keeping in mind that all the specimens have identical dimensions. Figure 14 summarizes the results of five single

pore specimens, each of them containing a centered inner pore of a varying diameter. Results for a fully dense specimen are also included for comparison. The fully dense and the Ø1 mm single pore specimens exhibit a similar behavior. The fully dense specimen's displacement is higher, but the force is surprisingly almost identical to that measured for the single pore specimen. It can be assumed that the reason for that is due to small differences between manufacturing batches. This can also indicate that the system is not sensitive enough for pore diameters smaller than Ø1 mm, or stated in terms of volume fraction, when the latter is of the order of 0.2%. However, a clear decline in the measured force can be seen, as the pore size increases. Since all the specimens failed in those tests, the reported displacement is the displacement to failure. The displacement decreases similarly, but more rapidly, as a function of the pore size. Figure 15 presents the results of Fig. 14, plotted this time as a function of pore volume fraction.

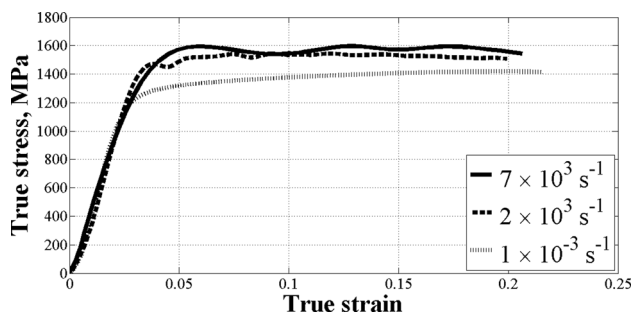


Fig. 13 Typical true stress–strain curve of printed Ti6Al4V at different strain rates. Note that once in the dynamic regime, the influence of the strain rate becomes minor. Note also the lack of strain hardening in the high rate regime.

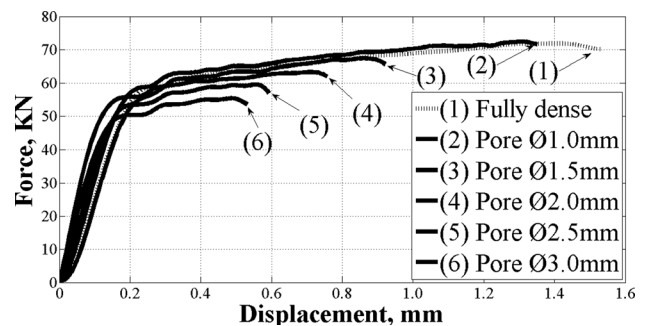


Fig. 14 Force as a function of displacement for different pore size. Note the decrease in load and displacement to failure as the pore diameter increases.

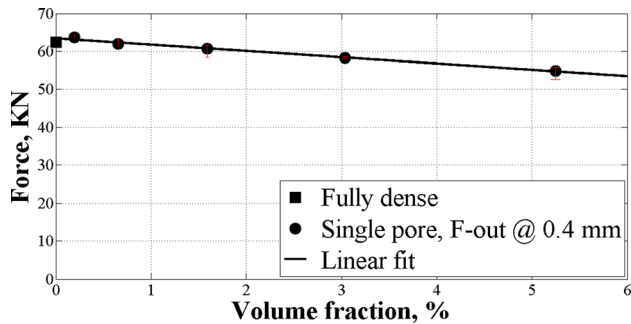


Fig. 15 Force as a function of volume fraction for a single pore specimen. The displacement is arbitrarily fixed to 0.4 mm.

The force was measured at 0.4 mm displacement, such as to allow for comparison.

From Fig. 15, it appears that the force and pore volume fraction are linearly related. The linear fit line predicts a force for the 0% pore volume fraction which is quite similar to the results of the fully dense material. The error bars show a high repeatability of the results. Figure 16 shows the shear failure mechanism of single pore specimens. Figure 17 shows a SEM image of one of the failed specimens that were shown in Fig. 16. As mentioned earlier, it was assumed that failure of specimen occurs before the residual powder is compressed and begins to affect the results. Figure 18 shows the boundary between the fully dense area and the single pore area. It is clear that the fully dense side was subjected to shear as indicated by elongated dimples, while the other side shows no shear signs. This finding is evidence that the trapped powder inside the pore has a negligible influence (if any) on the deformation of the specimen.

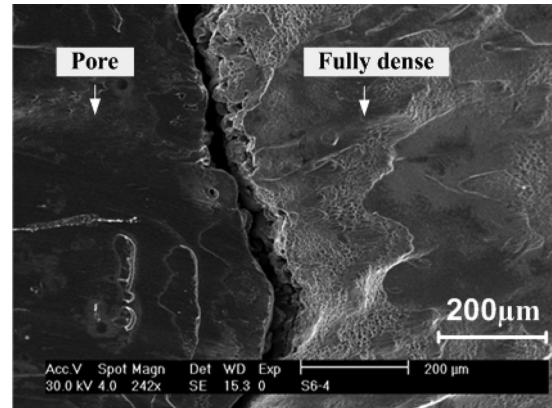


Fig. 18 SEM image of a single pore specimen failure

3.4 Dynamic Compression of Double Pore Specimen. The behavior of a single pore was performed using a specimen in which the pore is located at its geometric center. It was shown that the output force (F-out) is linearly related with the volume fraction of one centered spherical void. To assess the validity of these results for more than one pore, a set of double pored specimens was tested. As mentioned before, the volume fraction of the double pored specimens was kept equal to the volume fraction of single pored specimens. Three kinds of double pored specimens were tested, in which pores were oriented *axial*, *lateral*, and *diagonal*. For each orientation, three kinds of *d/B* ratio were tested. Figures 19(a)–19(c) describe the measured load–displacement curves at all orientations for a fixed *d/B* ratio of 1, 2, and 4, respectively. Significant differences related to the orientations of

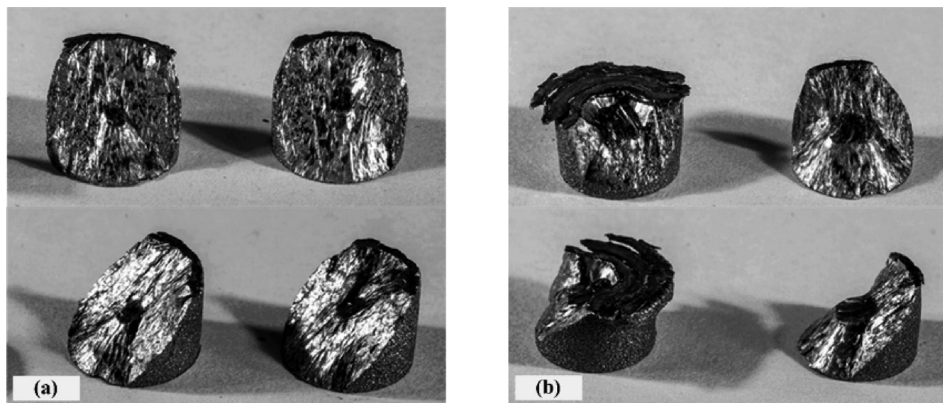


Fig. 16 Failure of a single pore specimen. (a) Pore Ø1 mm and (b) pore Ø2 mm.

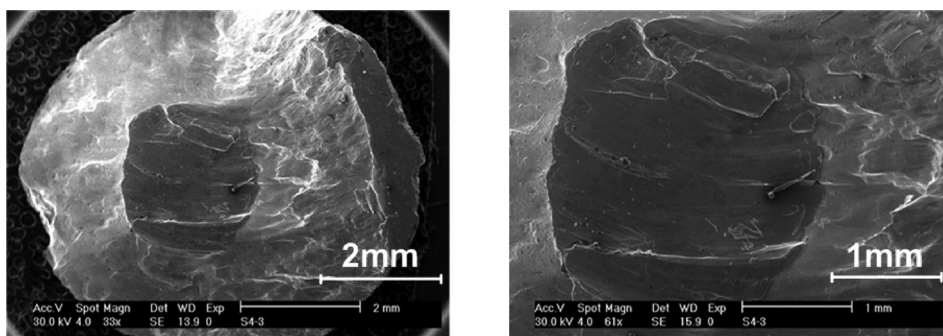


Fig. 17 SEM image of a single pore specimen failure at Ø2 mm pore size

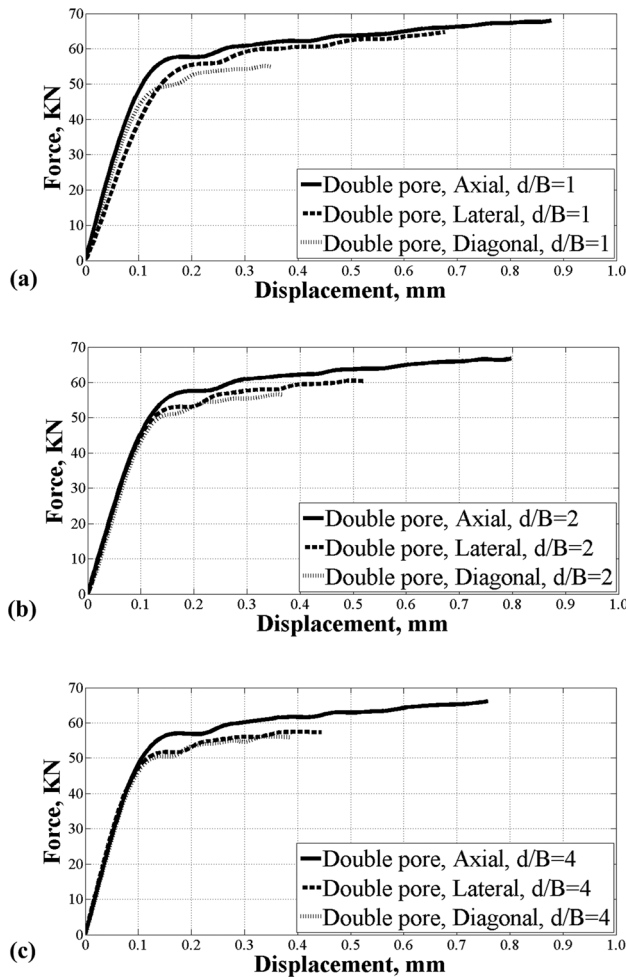


Fig. 19 Dynamic compression of double pored specimen in all orientations. (a) $d/B = 1$, (b) $d/B = 2$, and (c) $d/B = 4$.

the pores are clearly noticeable at each d/B ratio. While the axial direction exhibits the highest values of load and elongation, the diagonal direction has the lowest values. This trend remains constant regardless of d/B ratio. The values of the lateral pored specimens fall between the axial and the diagonal values. For high d/B ratio (pores are quite close), the lateral and the diagonal tend to behave similarly, while at low d/B ratio (pores are quite far), the differences between specimen's types is most significant, especially regarding their elongation to fracture. Figures 20(a)–20(c) describe measured load–displacement curves at all d/B ratio, each direction separately. For the axial direction, the differences in strength and elongation are minor. A similar behavior is observed for the diagonal direction, but significantly lower values of load and displacement were observed in this ratio. Unlike the results of those directions, the lateral direction shows noticeable differences in both parameters, depending on the d/B ratio. Figure 21 shows a summary of Figs. 19 and 20, as it describes the output force as a function of the volume fraction. The single pore results for specific volume fraction $f = 1.6\%$ are compared to the double pore results for all orientations and ratios.

The output force values of the axial double pored specimens are similar to those of the centered single pore, which both have the same volume fraction. Unlike that, the diagonal double pore specimens exhibit lower force values, compared to the single pored specimens, by about 10%. In the lateral double pored specimens, the matching to the single pored specimen's results (of force) seems to be related to the d/B ratio. It should be noted that the linear fit line of the single pored specimen intersects the force axis (at 0% volume fraction), almost at the same point that

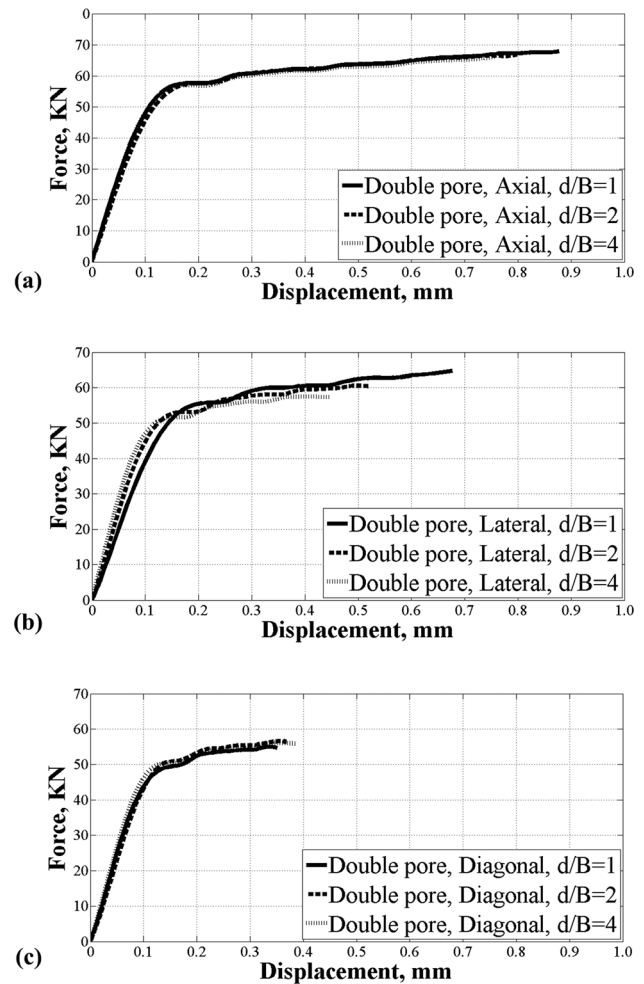


Fig. 20 Dynamic compression of double pore specimen in all d/B ratios. (a) Axial, (b) lateral, and (c) diagonal.

indicates the fully dense specimens results. Figure 22 shows a SEM image of a diagonal double pore specimen failure.

4 Discussion

The compressive strength of AM Ti6Al4V is found to be significantly higher compared to same material processed by conventional fabrication. While this result cannot be generalized to other AM materials, it is nevertheless a positive indication about the quality of the manufactured products. The originality of this work lies in the investigation of specimens with controlled closed porosity content. For this purpose, the AM technology was found to be ideal too. It should be noted that only discrete cases of porosity were examined, assuming they describe a single unit cell in an array of pores, such as centered spherical pore inside a cylindrical specimen. A similar idea has been suggested before by Tvergaard [9], who describes a model of ductile material containing centered spherical voids in array of hexagonal cell. The results of the single pored specimens reveal a strong linear relationship between force and volume fraction. As the volume fraction increases, the force declines moderately while ductility diminishes quite drastically. A comparison between single and double pored specimen, both with the same overall volume fraction, was found to be orientation dependent. Two *axial* pores behave similar to a centered single pore, almost without dependency of the distance between the pores. On the contrary, two *diagonal* pores are apparently promoting the shear failure much more than a centered single pore. Biswas and Ding [14] compared numerically a single pore and arrays of pores, and found that more pores will result in

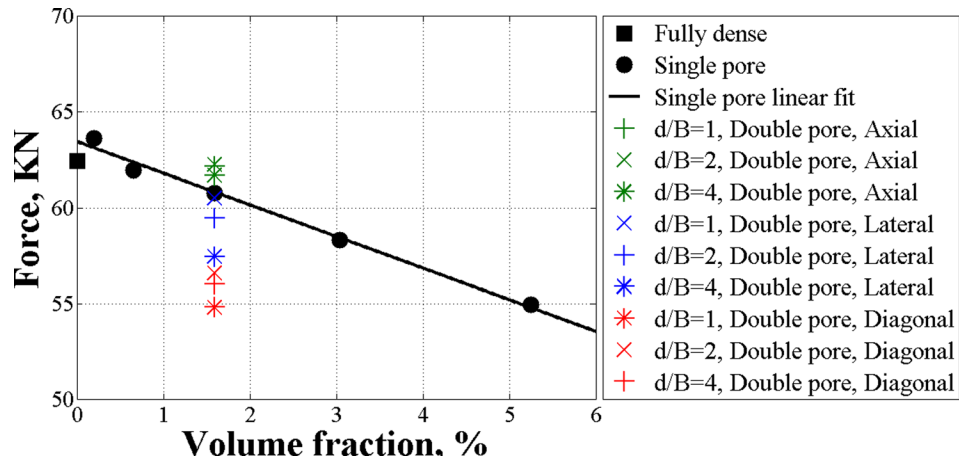


Fig. 21 Dynamic compression of single pore compared to double pore with 1.6% volume fraction at 0.4 mm elongation

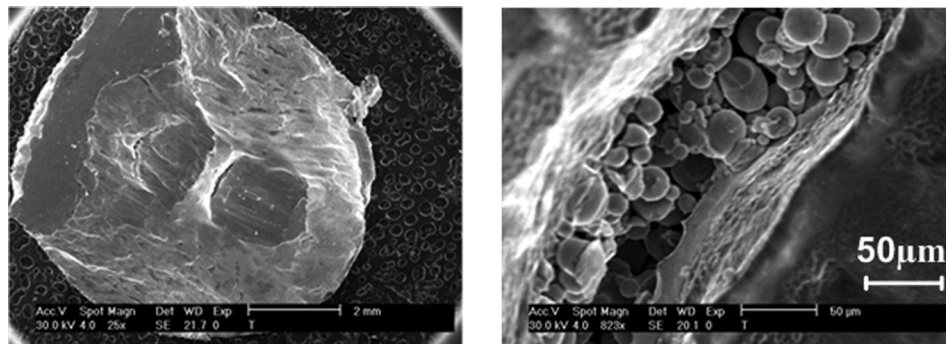


Fig. 22 SEM image of a diagonal double pore specimen failure. Note the remained powder, which can be related to the rapid failure.

Table 3 A summary of the results for the double pore specimens. (+) indicates a strong effect of the variable on load and elongation, compared to the results of the single pore specimens.

Variables	Load	Elongation
Orientation of pores (axial, lateral, diagonal)	Diagonal (+)	Diagonal (+)
	Lateral (+/-)	Lateral (+/-)
	Axial (-)	Axial (-)
<i>d/B</i> ratio (pore diameter divided by the distance between the pores)	Lateral (+)	Lateral (+)
	Axial (-)	Axial (-)
	Diagonal (-)	Diagonal (-)

faster failure propagation due to rapid void coalescence. The behavior of two pores in the *lateral* direction (compared to a single pore) is found to be dependent on the distance between pores. This dependency needs further investigation, as it does not appear explicitly in the above-mentioned failure criteria for porous materials. Indeed, in Gurson's model [8], the volume fraction of pores is the only microstructural variable [7,8]. Extensions of this model suggested adding parameters, such as void interaction effects [9], strain hardening effects [21], kinematic hardening [22], void nucleation, and coalescence [23,24]. The current research clearly suggests that the pores' orientation with respect to the load direction should also be considered as an important parameter to be included in the models of porous materials, as summarized in Table 3.

5 Conclusions

The mechanical properties of AM dense and porous Ti6Al4V specimens were investigated under static and dynamic compression.

- The compressive strength of AM Ti6Al4V is found to be significantly higher compared to same material processed by conventional fabrication.
- The dynamic behavior of the AM Ti6Al4V exhibits better performance in strength as compared to the conventionally processed material.
- The AM technology was found to be ideal for the investigation of specimens with controlled closed porosity content.
- The results of the single pored specimens reveal a strong linear relationship between force and pore volume fraction.
- A comparison between single pored and double pored specimens, both with the same overall volume fraction, was found to be strongly orientation dependent.
- The current research suggests that the pores' orientation with respect to the load direction should also be considered as an important parameter to be included in analytical failure models of porous materials.

References

- [1] Veiga, C., Davim, J. P., and Loureiro, A. J. R., 2012, "Properties and Applications of Titanium Alloys: A Brief Review," *Rev. Adv. Mater. Sci.*, **32**(2), pp. 133–148.
- [2] Nicholas, T., 1980, "Dynamic Tensile Testing of Structural Materials Using a Split Hopkinson Bar Apparatus," Air Force Wright Aeronautical Laboratories

- (AFSC), Wright-Patterson Air Force Base, OH, Report No. AFWAL-TR-80-4053.
- [3] Wulf, G. L., 1979, "High Strain Rate Compression of Titanium and Some Titanium Alloys," *Int. J. Mech. Sci.*, **21**(12), pp. 713–718.
 - [4] ASTM, 2014, "Standard Specification for Additive Manufacturing Titanium-6 Aluminum-4 Vanadium With Powder Bed Fusion," ASTM International, West Conshohocken, PA, Standard No. F2924-14, available at: <http://www.astm.org/Standards/F2924.htm>
 - [5] Gu, D. D., 2012, "Laser Additive Manufacturing of Metallic Components: Materials, Processes and Mechanisms," *Int. Mater. Rev.*, **57**(3), pp. 133–164.
 - [6] Kruth, J.-P., 2005, "Binding Mechanisms in Selective Laser Sintering and Selective Laser Melting," *Rapid Prototyping J.*, **11**(1), pp. 26–36.
 - [7] Benzerga, A. A., and Leblond, J., 2010, "Ductile Fracture by Void Growth to Coalescence," *Adv. Appl. Mech.*, **44**, pp. 169–305.
 - [8] Gurson, A. L., 1977, "Continuum Theory of Ductile Rupture by Void Nucleation and Growth: Part I—Yield Criteria and Flow Rules for Porous Ductile Media," *ASME J. Eng. Mater. Technol.*, **99**(1), pp. 2–15.
 - [9] Tvergaard, V., 1982, "On Localization in Ductile Materials Containing Spherical Voids," *Int. J. Fract.*, **18**(4), pp. 237–252.
 - [10] Nahshon, K., and Hutchinson, J. W., 2008, "Modification of the Gurson Model for Shear Failure," *Eur. J. Mech. A. Solids*, **27**(1), pp. 1–17.
 - [11] Xue, Z., Faleskog, J., and Hutchinson, J. W., 2013, "Tension–Torsion Fracture Experiments—Part II: Simulations With the Extended Gurson Model and a Ductile Fracture Criterion Based on Plastic Strain," *Int. J. Solids Struct.*, **50**(25–26), pp. 4258–4269.
 - [12] da Silva, M. G., and Ramesh, K. T., 1997, "The Rate-Dependent Deformation and Localization of Fully Dense and Porous Ti-6Al-4V," *Mater. Sci. Eng., A*, **232**(1–2), pp. 11–22.
 - [13] Biswas, N., Ding, J. L., and Balla, V. K., 2012, "Deformation and Fracture Behavior of Laser Processed Dense and Porous Ti6Al4V Alloy Under Static and Dynamic Loading," *Mater. Sci. Eng., A*, **549**, pp. 213–221.
 - [14] Biswas, N., and Ding, J., 2014, "Numerical Study of the Deformation and Fracture Behavior of Porous Ti6Al4V Alloy Under Static and Dynamic Loading," *Int. J. Impact Eng.* (in press).
 - [15] Kolsky, H., 1949, "An Investigation of the Mechanical Properties of Materials at Very High Rates of Loading," *Proc. Phys. Soc., London, Sect. B*, **62**(11), p. 676.
 - [16] Davies, E. D. H., 1963, "The Dynamic Compression Testing of Solids by the Method of the Split Hopkinson Pressure Bar," *J. Mech. Phys. Solids*, **11**(3), pp. 155–179.
 - [17] Ramesh, K. T., 2008, "High Rates and Impact Experiments," *Springer Handbook of Experimental Solid Mechanics*, Springer, New York, pp. 929–960.
 - [18] Sano, T., Kato, K., and Takeishi, H., 1995, "Analysis of Dynamic Deformation Mechanisms in Powder Metals," *J. Mater. Process. Technol.*, **48**(1–4), pp. 391–397.
 - [19] Peirs, J., Tirry, W., and Amin-Ahmadi, B., 2012, "Microstructure of Adiabatic Shear Bands in Ti6Al4V," *Mater. Charact.*, **75**, pp. 79–92.
 - [20] Osovski, S., Nahmany, Y., and Rittel, D., 2012, "On the Dynamic Character of Localized Failure," *Scr. Mater.*, **67**(7–8), pp. 693–695.
 - [21] Leblond, J.-B., Perrin, G., and Devaux, J., 1995, "An Improved Gurson-Type Model for Hardenable Ductile Metals," *Eur. J. Mech. A. Solids*, **14**(4), pp. 499–527.
 - [22] Mear, M. E., and Hutchinson, J. W., 1984, "Influence of Yield Surface Curvature on Flow Localization in Dilatant Plasticity," *Mech. Mater.*, **4**(3–4), pp. 395–407.
 - [23] Perrin, G., and Leblond, J. B., 1990, "Analytical Study of a Hollow Sphere Made of Plastic Porous Material and Subjected to Hydrostatic Tension—Application to Some Problems in Ductile Fracture of Metals," *Int. J. Plast.*, **6**(6), pp. 677–699.
 - [24] Benzerga, A. A., Besson, J., and Pineau, A., 1999, "Coalescence-Controlled Anisotropic Ductile Fracture," *ASME J. Eng. Mater. Technol.*, **121**(2), pp. 221–229.